



OPEN ACCESS

EDITED BY

Qiyang Tan,
The University of Queensland, Australia

REVIEWED BY

Erlei Li,
The University of Queensland, Australia
Guanyu Deng,
The University of Queensland, Australia

*CORRESPONDENCE

Xuewei Fang,
✉ xueweifang@xjtu.edu.cn
Jiyuan Zhao,
✉ 20222607@bistu.edu.cn

RECEIVED 25 April 2023

ACCEPTED 29 June 2023

PUBLISHED 19 July 2023

CITATION

Zhang Y, Fang X, Zhang W, Guo W,
Wang Z and Zhao J (2023), Molten pool
flow behavior and influencing factors in
electron beam selective melting of
IN738 superalloy.
Front. Mater. 10:1211648.
doi: 10.3389/fmats.2023.1211648

COPYRIGHT

© 2023 Zhang, Fang, Zhang, Guo, Wang
and Zhao. This is an open-access article
distributed under the terms of the
[Creative Commons Attribution License
\(CC BY\)](https://creativecommons.org/licenses/by/4.0/). The use, distribution or
reproduction in other forums is
permitted, provided the original author(s)
and the copyright owner(s) are credited
and that the original publication in this
journal is cited, in accordance with
accepted academic practice. No use,
distribution or reproduction is permitted
which does not comply with these terms.

Molten pool flow behavior and influencing factors in electron beam selective melting of IN738 superalloy

Yihui Zhang¹, Xuewei Fang^{1*}, Wannian Zhang¹, Wenhua Guo¹,
Zhixiang Wang² and Jiyuan Zhao^{3*}

¹The State Key Laboratory for Manufacturing Systems Engineering, Xi'an Jiaotong University, Xi'an, Shaanxi, China, ²National Innovation Institute of Additive Manufacturing, Xi'an, Shaanxi, China, ³School of Automation, Beijing Information Science and Technology University, Beijing, China

Electron beam selective melting (EBSM) has emerged as a promising technology for additive manufacturing (AM) of superalloys. In this study, a comprehensive multi-physics model is developed to analyze the molten pool flow behavior and influencing factors in the EBSM process. The discrete element method (DEM) and volume of fluid (VOF) method are employed to establish the powder bed model and track the solid-liquid free surface, respectively. The results reveal that the molten pool exhibits a conduction mode characterized by a large width-to-depth ratio driven by the Marangoni effect. Internal vortices cause the molten pool to expand even after the scan ends. The ambient pressure, in comparison to the preheat temperature, has a significant impact on vapor recoil and consequently affects the surface quality of the molten pool. Moreover, a large hatch distance results in cracks and porous morphological features on the surface of the samples. These findings demonstrate the effectiveness of numerical simulations in providing detailed insights into the EBSM process of the IN738 superalloy material.

KEYWORDS

electron beam selective melting, superalloy, numerical simulation, molten pool behavior, influencing factors

1 Introduction

Electron beam selective melting (EBSM) is a powder bed fusion technique based on discrete stacking. It utilizes an electron beam as a heat source to melt metal powder and create parts. Unlike other additive manufacturing (AM) technologies, EBSM is typically conducted in a vacuum environment with high preheating temperatures. This approach reduces the residual stress in the parts. EBSM offers several advantages, including fast molding speed, high efficiency, optimal energy utilization, and excellent mechanical properties of the molded parts. As a result, it finds extensive applications in aerospace, biomedical, and other industries (Al-Bermani et al, 2010) (Murr et al, 2010) (Tan et al, 2015). However, despite its many benefits, EBSM encounters issues during the production process, such as spattering, balling, unfusion, and cracking, which ultimately impact the final product

quality (Tumbleston et al, 2015). Due to the closed high-temperature vacuum chamber and the rapid movement of the electron beam during printing, explaining the complex physical phenomena and the swift evolution of thermal behavior in EBSM using experimental methods proves challenging.

The advent of computational materials science has led to the widespread use of numerical simulation in the field of AM. Numerous studies have emphasized the importance of numerical simulation in understanding and optimizing the EBSM process (Qi et al, 2007) (Zäh and Lutzmann, 2010) (Cheng and Chou, 2013) (Wang et al, 2015) (Shen and Chou, 2012) (Riedlbauer et al, 2017). Nevertheless, conventional constitutive equations fail to accurately describe the intricate physical processes of AM at the macroscopic scale. Consequently, computational fluid dynamics (CFD) simulations must be extended to the mesoscale to achieve a more precise comprehension of the EBSM process. Generally, CFD simulations encompass solving nonlinear partial differential equations that govern the conservation of mass, momentum, and energy. These simulations extensively cover hydrodynamic effects (Khairallah et al, 2016) (Körner et al, 2011). Despite their high computational cost, CFD simulations provide a more realistic temperature history, thereby facilitating a better understanding of molten pool dynamics, solidification organization, and thermal stresses.

The forming quality of a single track is critical as it directly impacts the final surface quality and mechanical properties of the part. In a single track, fluid flow is associated with the formation of various defects, necessitating the study of fluid flow behavior and its influencing factors. Yan et al. (Yan et al, 2018) proposed a multi-physics field coupling algorithm for simulating balling and unevenness phenomena in Ti-6Al-4V single track molding. Lee et al. (Lee and Zhang, 2016) investigated the heat and mass transfer process of the IN718 alloy powder bed under the influence of a laser heat source. The results revealed a depressed area at the front of the recoil pressure and the flow of the molten pool to the back surface due to the Marangoni effect. Zhao et al. (Zhao et al, 2019) examined the flow behavior of the EBSM molten pool and the solidification conditions of the Co-Cr-Mo alloy. Their study indicated that active fluid convection at the solidification front increased the likelihood of new grain formation while inhibiting the epitaxial growth of columnar grains.

To date, simulations of EBSM have primarily focused on Ti-6Al-4V and IN718, with limited studies exploring other alloys, especially at the mesoscopic scale. The understanding of molten pool flow behavior and influencing factors for superalloy powders during the EBSM process remains insufficient. IN738 is a precipitation strengthened superalloy which is conventionally processed by casting. Due to its superior high temperature performances, IN738 is the most commonly used material for high pressure turbine since developed. Nevertheless, the higher Aluminum and Titanium contents make IN738 more prone to defects formation during rapid melting and solidification by EBSM compared with other Nickel-based superalloys. To eliminate the defects in the process of IN738 EBSM, researchers investigated the mechanism and variation of melting and solidification process of IN738 with different process parameters. However, the process window for IN738 is narrow and the cost of extensive trial-and-error experiments is very high. Therefore, it is valuable to

investigate the molten pool flow and effects through numerical methods.

This study aims to address this gap by developing a 3D transient mesoscopic model that predicts the thermal behavior, flow mechanism of the molten pool, and the formation of melted tracks during the EBSM process of the IN738 superalloy. The simulation incorporates a 3D Gaussian packed powder bed composed of spherical particles, created using the discrete element method (DEM), which considers the individual effects of powder particles. Additionally, volume shrinkage and temperature-dependent thermal physical parameters are considered. The tracking of the solid-liquid free surface is achieved using the volume of fluid (VOF) method. Furthermore, experimental investigations are conducted to examine the morphology of single and double tracks under different processing parameters. These experiments serve to verify the feasibility and reliability of the developed model.

2 Numerical simulations

The 3D transient simulation of the molten pool for IN738 particles involved three key steps: powder falling, spreading, and melting. These individual steps were addressed using two commercial software packages, namely, EDEM for powder falling and spreading, and FLOW-3D for the melting process.

2.1 Powder spreading model

The DEM was employed to construct the single-layer powder bed model. To achieve a more precise particle model, the morphological parameters of the powder were analyzed using both scanning electron microscopy (SEM) and laser granulometry. The IN738 powder utilized in this study was pre-alloyed and provided by the China Iron and Steel Research Institute Group. It was produced through a combination of vacuum induction melting and gas atomization with argon (Ar). The as-received powder exhibited predominantly spherical particles with numerous satellites, as depicted in Figure 1.

The particle model consisted of spherical particles with diameters distributed in a Gaussian fashion between 45 μm and 105 μm . The translational and rotational motions of individual powder particles can be described by Newton's second law of motion:

$$\begin{cases} m_i \frac{d^2 r_i}{dt^2} = m_i g + \sum_j (F_n + F_t + F_c) \\ I_i \frac{d^2 \theta_i}{dt^2} = \sum_j R_i \times F_t \end{cases} \quad (1)$$

Where m_i , I_i , R_i , r_i , and θ_i are the mass, moment of inertia, radius, position vector and angular displacement of particle i ; F_n , F_t and F_c are the normal contact force, tangential contact force and cohesion force.

To simulate the contact between particles, the Hertz-Mindlin soft-contact model (Xiang et al, 2016) was employed. This model permits overlapping at the contact point to simplify elastic deformation, as illustrated in Figure 2A. In this model, the normal contact force F_n and the tangential contact force F_t were calculated

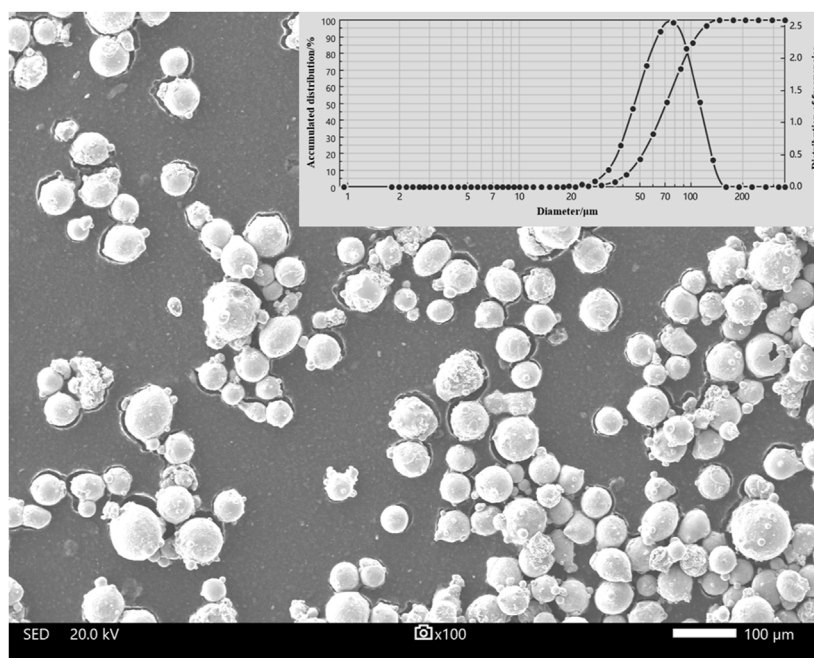


FIGURE 1
SEM morphology and particle size distribution of IN738 powder.

using the Hertz formula and the Coulomb friction law, respectively, as shown in Eqs 2, 3.

$$F_n = \frac{4}{3} E^* \sqrt{R^*} \delta_n^{\frac{3}{2}} \tag{2}$$

$$F_t = 8G^* \sqrt{R^*} \delta_n \delta_t \tag{3}$$

where E^* , R^* and G^* are the Young’s modulus, equivalent radius, and shear modulus, respectively. The δ_n and δ_t are the overlap in the normal and tangential.

When the particle size is below 100 μm , in addition to contact forces, Van der Waals forces (i.e., cohesion force F_c) also play an important role. In this study, we incorporated the influence of Van der Waals forces using the Johnson-Kendall-Roberts (JKR) model (Parteli and Pöschel, 2016).

$$F_{JKR} = -4\sqrt{\pi\gamma E^*} \alpha^{\frac{3}{2}} + \frac{4E^*}{3R^*} \alpha^3 \tag{4}$$

where γ is the surface energy and α is the radius of the contact area.

2.1.1 Model validation

To validate the accuracy of the model, the static repose angle was measured by the injection method and compared with experimental data. Figure 2B shows the model of the simulation. The particles were color-coded to represent different sizes, with red indicating the largest particles and blue representing the smallest ones. To reduce the computational effort, the whole model was reduced in equal scale. A funnel with a diameter of 8 mm was filled with particles, which accumulate on a plane 10 mm from the bottom of the funnel under the effect of gravity. To minimize errors, the simulations and

experiments were each carried out three times and averaged. Finally, the static repose angles measured by simulation and experiment are 32° and 34° respectively, with an error of 5.8%.

Subsequently, the simulated and experimental tap densities were compared. For this purpose, a rectangular container measuring 1 × 1 × 1.5 mm was filled with model particles. The container was then subjected to vibration at a frequency of 250 times per minute for a duration of 12 min, as depicted in Figure 2C. Table 1 lists the values of parameters employed in the simulations.

The tap density ρ_t is calculated using Eq. 5:

$$\rho_t = \frac{M}{V_a} \tag{5}$$

where M is the total mass of particles in the container, V_a is the apparent volume. The tap density of the model was measured to be 4.7 g/cm^3 using Eq. 4, which is close to the experimental tap density of 5 g/cm^3 with an error of 6%.

2.1.2 Powder bed model

The powder bed model was established in two distinct steps: powder falling and spreading. Initially, over 10,000 particles were generated approximately 2.5 mm above the substrate and allowed to fall freely under the influence of gravity, accumulating on the surface of the substrate. This resulting powder bed model is depicted in Figure 3A. It is worth noting that the height of the stacked particles exceeds the thickness of the printed layer, set at 100 μm in this case.

On the other side of the substrate, a DEM domain was employed to contain the powder bed model, as described in Section 2.2. Subsequently, a rigid rake was implemented to scrape and distribute

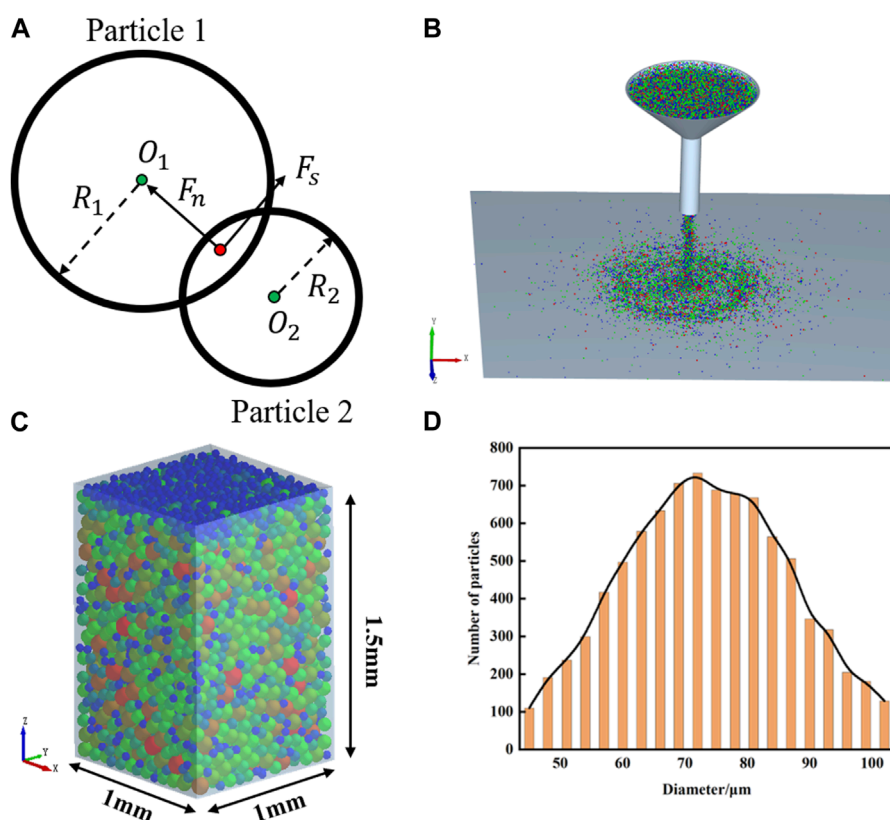


FIGURE 2

(A) The physics of particles contact. (B) The static repose angle model. (C) The tap density model, in which different colors represent different particle sizes. (D) The particle size distribution is approximately Gaussian distribution.

TABLE 1 The values of variables considered in the simulations.

Name	Symbol and unit	Value	Ref
Particle density	ρ (kg/m^3)	8500	Chun (2019)
Young's modulus of particles	E (MPa)	7.90E+10	
Poisson's ratio of particle	ξ	0.31	
Restitutions coefficient of particle/particle	e	0.42	
Sliding friction coefficient of particle/particle	μ_s	0.35	
Rolling friction coefficient of particle/particle	μ_r	0.01	

all the particles within the domain, simulating the powder spreading process. The velocity of the rake was set at approximately 200 mm/s, consistent with that employed in the actual EBSM process.

2.2 Powder melting model

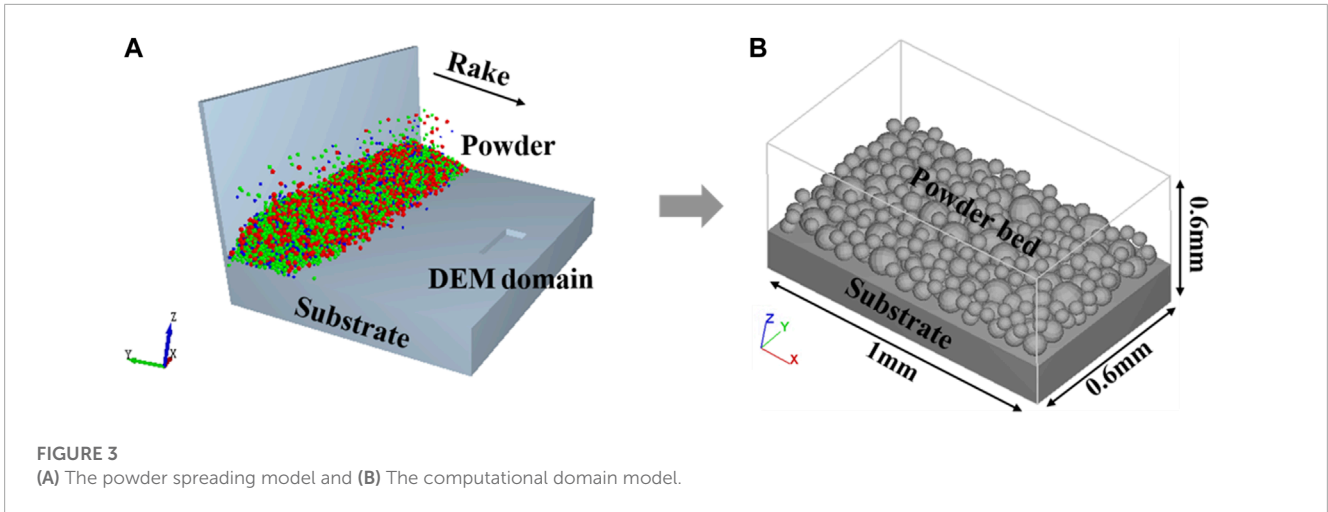
2.2.1 Computational domain

The computational domain dimensions were defined as follows: 1000 μm in length (X direction), 600 μm in width (Y direction),

and 600 μm in height (Z direction). A rectangular substrate with an equivalent surface area was created beneath the powder bed model, and its height was set at 300 μm , as depicted in Figure 3B.

For a typical simulation case in this study, approximately 2.69 million cells were generated using a finer mesh size of 5 μm . A mesh convergence test was performed to ensure that the model was not sensitive to the mesh.

The simulations were executed on a workstation equipped with an Intel® Xeon® Gold 6226 R processor and 128 GB of RAM. It required approximately 168 h of CPU clock time to complete the calculation of a physical process that lasted 6 ms.



2.2.2 Governing equations

The EBSM is a complex fluid dynamics process, involving the heating, melting, flow, evaporation, and solidification of powders. The molten metal is assumed to be an incompressible Newtonian fluid throughout the simulation. Generally, the dynamic flow field within the molten pool is governed by Navier-Stokes and energy equations, which can be expressed as follows:

$$\text{Mass: } \nabla \cdot \vec{v} = 0 \tag{6}$$

$$\text{Momentum: } \frac{\partial \vec{v}}{\partial t} + (\vec{v} \cdot \nabla) \vec{v} = -\frac{1}{\rho} \nabla P + \mu \nabla^2 \vec{v} + \vec{g} [1 - \beta(T - T_m)] \tag{7}$$

$$\text{Energy: } \frac{\partial h}{\partial t} + (\vec{v} \cdot \nabla) h = \frac{1}{\rho} (\nabla \cdot \lambda \nabla T) + q \tag{8}$$

where \vec{v} is the velocity of the fluid, t is time, ρ is the density, p is the pressure, μ is the viscosity, g is the gravitational acceleration, β is the thermal expansion coefficient, T is the temperature, T_m is the melting temperature of material, h is the enthalpy and λ is the thermal conductivity. Q is the Gaussian heat source of electron beam.

The position of the free surface between the void and the molten pool was tracked using the VOF method. The VOF function, originally derived by Hirt and Nichols (Hirt and Nichols, 1981), is defined by Eq. (9):

$$\frac{\partial F}{\partial t} + \nabla \cdot (\vec{v}F) = 0 \tag{9}$$

where F is the fluid volume function, which represents the fraction of the volume fraction of the liquid metal filled in the cell. $F = 1$ indicates that the grid is full of liquid, and $F = 0$ is completely empty. $0 < F < 1$, suggesting that the grid is on a free surface.

2.2.3 Boundary conditions

As discussed earlier, EBSM is a complex process that involves multiple factors, including the input of electron beam, heat absorption by the powder bed, heat dissipation through radiation, and heat carried away by melt evaporation. The heat input from the electron beam, which is applied to the top free surface of the

powder layer, is modeled as a Gaussian distribution across the surface.

$$q = \frac{3\eta P}{\pi r^2} \exp\left(-\frac{3w^2}{r^2}\right) \tag{10}$$

where η is the electron beam absorptivity of the IN738, p is the electron beam power, r is the effective electron beam radius and w is the radial distance from the beam center.

Because the EBSM process takes place in a high vacuum environment (0.1 Pa), heat convection loss is negligible. Therefore, only heat loss from thermal radiation and evaporation need to be considered in the simulation. The thermal radiation is governed by the Stefan-Boltzmann law:

$$j^* = \epsilon \sigma (T^4 - T_0^4) \tag{11}$$

where ϵ is the material emissivity, σ is the Stefan-Boltzmann constant and T_0 is the ambient temperature.

During the EBSM process, the surface temperature of the molten pool can reach the boiling temperature of the material. As a result, the metal vapor carries away a portion of the heat and exerts recoil pressure on the molten pool. The heat loss of the metal vapor can be described as follows (Cho et al, 2009):

$$q_{evap} = \frac{0.82 \Delta H_v^*}{\sqrt{2\pi MRT}} P_0 \exp\left(\frac{\Delta H_v^* (T - T_b)}{RTT_b}\right) \tag{12}$$

where M is the molar mass, R is the universal gas constant, T_b is the boiling temperature and ΔH_v^* is the effective enthalpy, which can be defined as:

$$\Delta H_v^* = \Delta H_v + \frac{k(k+1)RT}{2(k-1)} \tag{13}$$

where ΔH_v is latent heat of vaporization and k is the adiabatic index.

In order to accurately solve the fluid flow, this simulation considers two main driving forces. The first force is the Marangoni shear stress induced by the temperature-dependent surface tension force:

$$\gamma(T) = \gamma_L + \frac{d\gamma}{dT} (T - T_L) \tag{14}$$

TABLE 2 Thermophysical properties of IN738 and coefficients and constants applied to the simulation.

Name	Symbol and unit	Value	Ref
Emissivity	ϵ	0.6	Risse and Broeckmann (2019)
Liquidus temperature	T_L (K)	1623	Khairallah and Anderson (2014)
Solidus temperature	T_S (K)	1533	
Boiling point at standard atmospheric pressure	T_b (K)	3223	
Latent heat of fusion	ΔH_f (J/kg)	3.0e+05	
Latent heat of vaporization	ΔH_v (J/kg)	6.7e+06	
Adiabatic index	k	1.4	Zhao et al (2019)
Stefan-Boltzmann constant	σ (W/m ² ·K ⁴)	5.67e-08	—
Universal gas constant	R (J/K·mol)	8.314	—
Environment temperature	T_0 (K)	700	—
Energy efficiency	η (%)	90	—
Temperature coefficient of surface tension	$\frac{dy}{dT}$ (J/m ² ·K)	-0.00011	—

where γ_L is the surface tension at the liquidus and $\frac{dy}{dT}$ is the temperature coefficient of surface tension.

The second force is the recoil pressure caused by metal material evaporation and is expressed in Eq. (15):

$$P_r = 0.54P_0 \exp\left(\frac{\Delta H_v(T - T_b)}{RTT_b}\right) \quad (15)$$

where P_0 is ambient pressure, 0.54 is the calibration coefficient and suggests that 54% of the vapor pressure is equal to the recoil pressure (Allmen and Blatter, 2013).

The physical properties of IN738 superalloy and the coefficients/constants used in the simulation are listed in Table 2. The temperature-dependent material properties, including thermal conductivity, specific heat (Yann et al, 2010) (Kerrouault, 2000), density (Chapman et al, 2008), viscosity and surface tension (Aune et al, 2005), are illustrated in Figure 4.

3 EBSM experiment

The powder melting model was validated through a series of experimental melting trials. Initially, a simple cubic coupon measuring 30 mm × 30 mm × 5 mm was built on a flat 316 L substrate using an Arcam[®] A2X machine. Single tracks were then constructed on the surface of the coupons, perpendicular to the direction of powder spreading. Subsequently, several cubic block samples with dimensions of 15 mm × 15 mm × 10 mm were produced to investigate the impact of hatch on the densification rate and surface roughness.

During the EBSM process, a vacuum pressure of 0.1 Pa was maintained within the process chamber, and the substrate was preheated to 1273 K, which represents the standard preheating temperature for the IN738 superalloy. The utilized power (p) was calculated as the product of the acceleration voltage (60 kV) and beam current. The specific process parameters employed in the experiments are detailed in Table 3.

To examine the morphology and profile of the melt track, a digital microscope (KEYENCE, VHX-950F, Japan) was utilized. The method employed for measurement is illustrated in Figure 5. The samples were prepared by wire-cutting perpendicular to the scanning direction, followed by grinding and polishing using standard metallographic techniques. The surface topography of the samples was then assessed using a laser confocal scanning microscope (LSCM, Smartproof 5, Zeiss), and the surface roughness was expressed as Sa. Furthermore, the densities of the samples were measured using the Archimedes method.

4 Results and discussion

4.1 Molten pool dynamics and morphologies

Figure 6 illustrates the temperature fields and time-dependent morphology of the molten pool during single track scanning at $p = 300$ W and $v = 1.0$ m/s. The computational domain is divided along the X-Z plane at the center of the track, revealing the temperature profile across the substrate. The molten pool is represented by the red region, which encompasses temperatures at or above the liquidus temperature ($T_L = 1623.15$ K).

In the initial stage (Figure 6A), the powder and substrate swiftly absorb energy from the high-speed electrons, reaching the melting point in a short duration. Subsequently, the powder and substrate melt and blend together, forming a molten pool with intricate flow patterns induced by Marangoni forces, recoil pressure, gravity, and buoyancy (Figure 6B). Toward the end of the scanning process (Figure 6C), the width and depth of the molten pool head exceed those of the tail due to heat accumulation. Subsequently, owing to the high surface tension and low viscosity of the liquid metal, the molten pool exhibits highly dynamic fluctuations, progressively melting the surrounding powder and expanding to its maximum volume (Figure 6D). Finally, as the

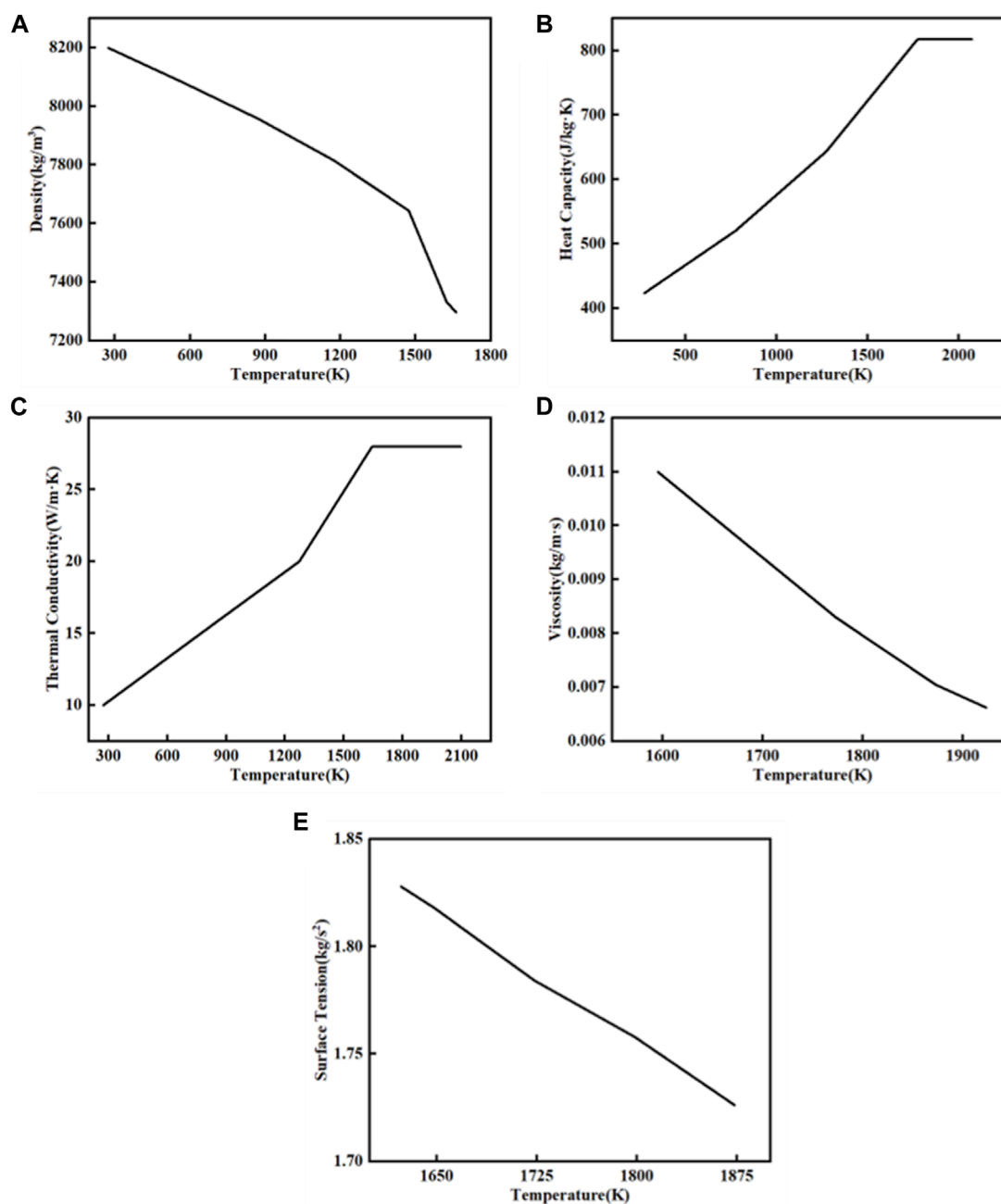


FIGURE 4 Temperature-dependent thermo-physical properties of IN738, (A) Density, (B) Heat capacity, (C) Thermal conductivity, (D) Viscosity and (E) Surface tension.

temperature decreases, the molten pool solidifies, resulting in an irregular appearance (Figure 6F).

It is noteworthy that the melting and solidification process of the EBSM molten pool significantly differs from that of Selective Laser Melting (SLM). In SLM, the molten pool typically solidifies rapidly following the laser scan. However, in EBSM, the molten pool continues to expand for an extremely brief period after the scanning ends. This behavior primarily arises from the higher preheating temperature in EBSM, which enhances the material's

thermal conductivity (Leung et al, 2019). Additionally, the high energy density and absorption efficiency of the electron beam (up to 90%) (Boley et al, 2015), coupled with the absence of thermal convection loss, enable heat accumulation, facilitating the expansion of the molten pool.

Due to the random distribution of powder, the temperature field of the molten pool experiences unstable distribution during the EBSM process. Therefore, a probe point was selected ($X = 400 \mu\text{m}$, $Y = 200 \mu\text{m}$, Z located at the free surface) for observation within

TABLE 3 Combinations of processing parameters.

Process parameters	Value
Electron Beam Power (W)	120, 240, 480, 720
Scanning Speed (mm/s)	1, 2, 3, 4
Layer Thickness (mm)	0.1
Hatch (mm)	0.05, 0.10, 0.15, 0.20

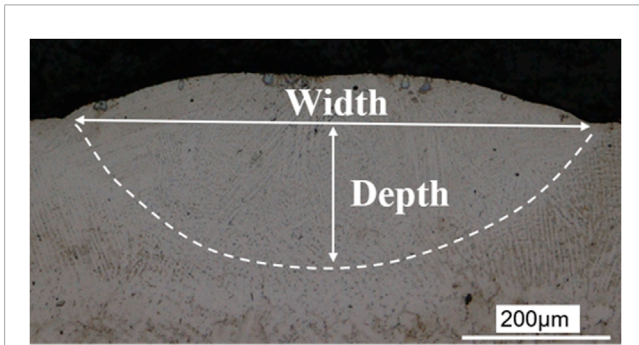


FIGURE 5 Method of determining dimensions.

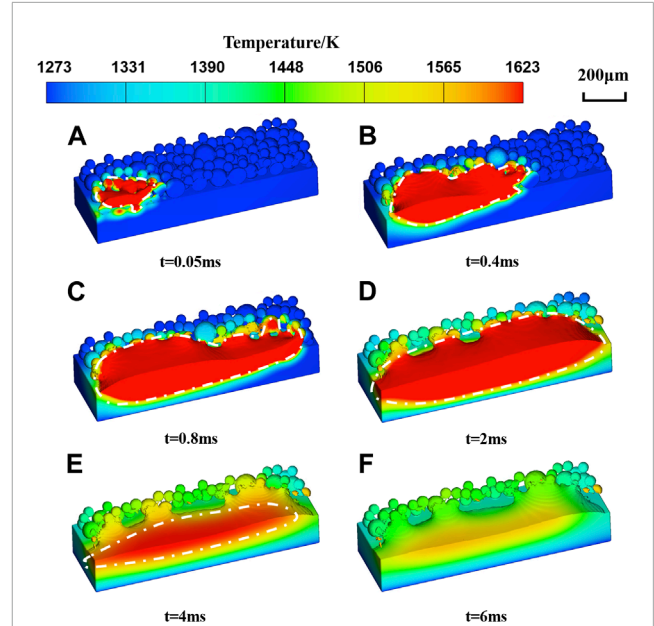


FIGURE 6 Temperature fields and morphologies of molten pool during scanning, (A) $t = 0.05$ ms, (B) $t = 0.4$ ms, (C) $t = 0.8$ ms, (D) $t = 2$ ms, (E) $t = 4$ ms and (F) $t = 6$ ms. (X-Z symmetry section computational domain; Electron beam scanning from left to right).

the melt pool. This point varies in the Z-axis with the free surface during melting and solidification accordingly. Figure 7 illustrates the variation of temperature (T), temperature gradient (G), and cooling rate (R) with time (t), where the scanning process occurs from 0 to 0.8 ms and the cooling process occurs from 0.8 to 6 ms. A negative cooling rate indicates the heating process, while a positive value represents the cooling process. The G and R can be expressed as Eqs 16, 17:

$$\begin{cases} G_i = \frac{\partial T}{\partial d} \\ G = \sqrt{G_x^2 + G_y^2 + G_z^2} \end{cases} \quad (16)$$

$$R = \frac{\partial T}{\partial t} \quad (17)$$

Where G_x, G_y and G_z are the components of the temperature gradient.

During the scanning process, the temperature rises rapidly before melting, while G and R remain relatively low, ranging from approximately 10^{-8} to 10^{-6} . As heat gradually transfers to the probe point, melting commences after the temperature surpasses the solidus temperature ($T_s = 1533$ K). Consequently, due to the latent heat at the moment of melting and the change in the direction of heat transfer, G and R undergo a significant and abrupt change, reaching values of 2.2×10^7 K/m and -3.8×10^7 K/s, respectively. Subsequently, they rapidly decrease, indicating that melting is a transient process. From 1.0 to 3.5 ms, the temperature gradually decreases with time, while G and R remain at low values. Around 3.5 ms, the temperature drops below the liquidus temperature ($T_L = 1623$ K), initiating the solidification of the molten pool. At almost the same moment, G and R rise sharply (reaching 9.8×10^7 K/m and 7.8×10^7 K/s, respectively), and then decline rapidly at the end of

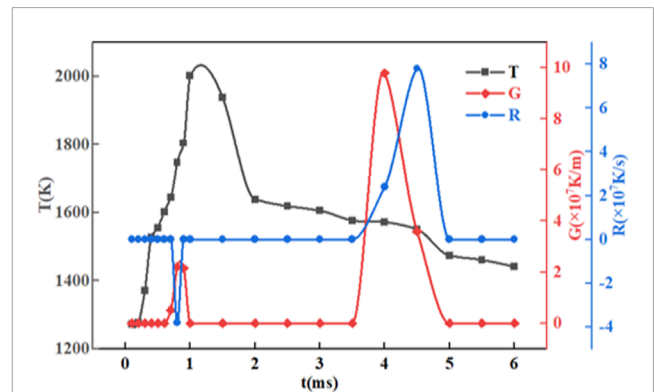


FIGURE 7 Variation of Temperature T, temperature gradient G and cooling rate R at probe point (X = 400 µm, Y = 200 µm, Z located at the free surface) with time t.

solidification. The aforementioned process reveals that the electron beam melting process is a non-equilibrium process characterized by “fast heating and cooling” at the moment of melting and solidification. G and R can reach magnitudes of 10^7 or higher. However, the entire molten pool experiences “fast heating and slow cooling,” with the temperature rising rapidly above the melting point for a brief period (the central region of the molten pool may exceed the boiling point) and subsequently gradually cooling down.

The flow behavior of the molten pool exhibits a similar trend to laser powder beds reported in the literature (Cheng et al, 2019) (Li et al, 2022), although they are not identical due to

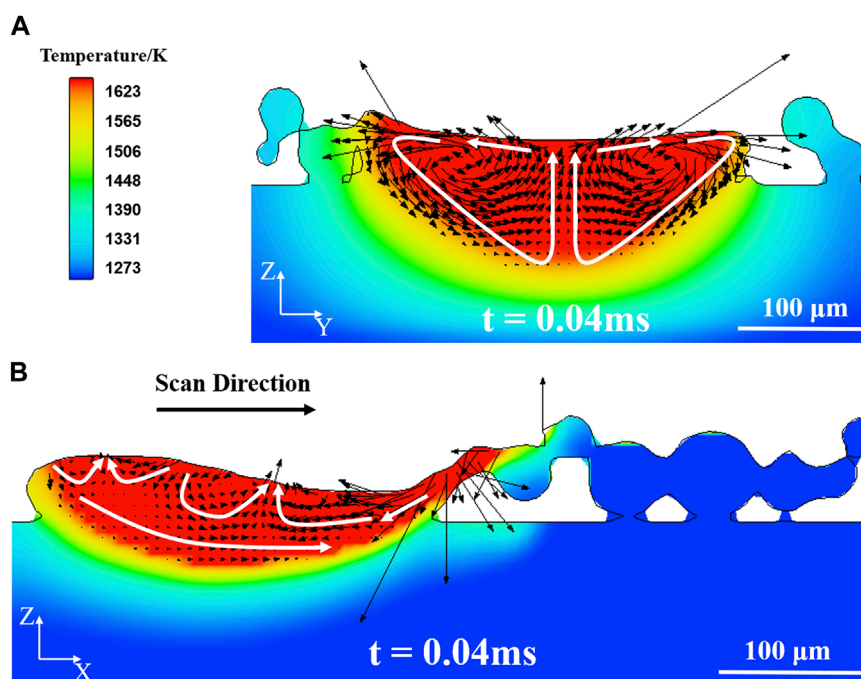


FIGURE 8
Molten pool flow behavior in YZ (A) and XZ (B) sections. The black arrows indicate the velocity vector. The schematic of the flow pattern is demonstrated by the white arrows.

the large width/depth ratio in EBSM (Zhao et al, 2020). Figure 8 demonstrates the complex flow behavior of the molten pool in the YZ and XZ sections. As depicted in Figure 8A, under the influence of Marangoni convection, the molten pool at the surface is drawn toward the interior, resulting in clockwise or counterclockwise vortices. Although this flow pattern can lead to defects such as porosity, cracks, balling, and sputtering, it also facilitates the expansion of the molten pool into the surrounding area.

Figure 8B illustrates the flow behavior along the scan direction. Due to surface tension, the molten liquid swiftly flows backward after the electron beam spot, encountering the re-solidification zone, and then reverses its direction to flow forward. Some of the forward-flowing liquid collides and rotates with the newly generated backward liquid in the central region of the molten pool, ultimately converging and flowing upward. Another portion flows forward along the bottom of the molten pool, filling the depressed area.

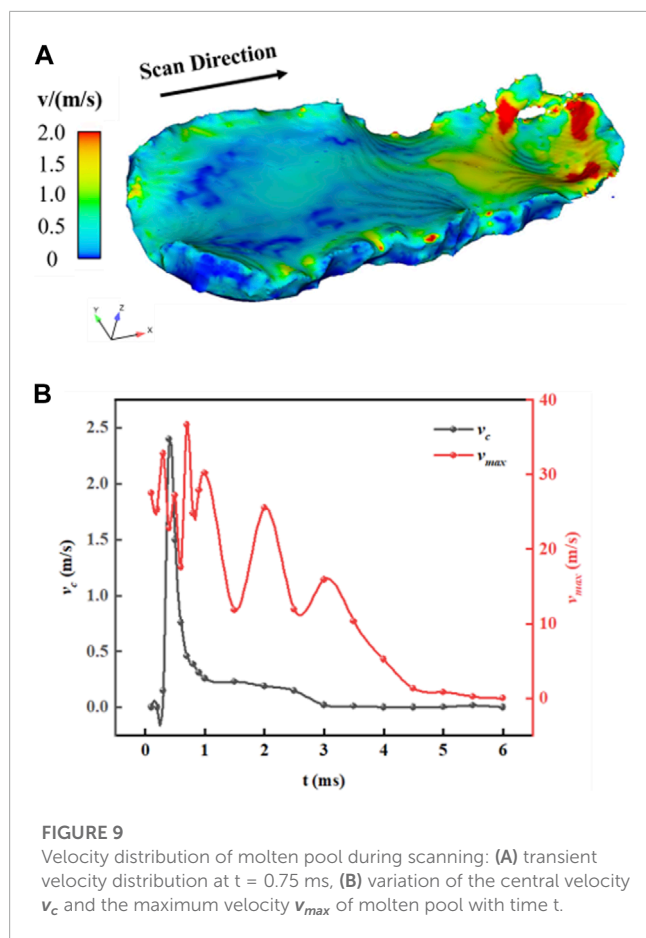
The flow behavior of the molten pool is a result of the combined effects of several forces, including surface tension, Marangoni force, vapor recoil pressure, and electron counter pressure, among others. According to a study by Zhao et al (Zhao et al, 2019), Marangoni convection primarily influences the profile and temperature distribution of the molten pool. Figure 9A illustrates the velocity distribution of the liquid metal during the scanning process ($t = 0.75$ ms). In the region where the electron beam impacts, the high-temperature gradient generates intense Marangoni convection, leading to rapid flow of the molten pool. Additionally, due to the irregular shape of the powder particles, the velocity at the edges of the molten pool is greater than that in the inner region. Figure 9B presents the variation of the central velocity

v_c and maximum velocity v_{max} of the molten pool over time. The v_c reaches its maximum when the beam spot passes, and then rapidly decreases. However, the v_{max} fluctuates significantly throughout the process and remains considerably higher than v_c . This indicates that the flow velocity of the molten pool is not uniform. In the region with a high-temperature gradient, the liquid metal in the molten pool flows at a high speed for a brief period, driven by the Marangoni force.

4.2 Effect of environment conditions

In the actual production process, the vacuum environment of EBSM can reduce the interference of impurities in the gas with the high-speed electron beam. The high preheating temperature can pre-sinter the powder in advance and prevent powder smoke. Besides, during the interaction between the energy beam and the material, the keyhole formation is usually associated with the recoil pressure caused by the evaporation of the metal. The high vacuum environment within the EBM can significantly attenuate the effect of the vapor recoil pressure. Therefore, it is worthwhile to study the influence of ambient pressure on the keyhole and the molten pool flow. However, studying the effect of changing environmental conditions on the molten pool experimentally is difficult, and it is discussed next from the perspective of simulation.

Based on Section 4.1, simulations were performed for the no-preheat temperature ($T = 300$ K, Figure 10B) and standard atmospheric pressure (101,325 Pa, Figure 10C), respectively, by changing environmental conditions. It should be noted that, under



standard atmospheric pressure, the substrate thickness was doubled to avoid being penetrated by the molten pool, which does not affect the heat transfer effect. As shown in Figure 10, the maximum temperature of the molten pool is above the material boiling point ($T_b = 3223$ K) for all three environmental conditions. Compared to the normal conditions (case (a)), the temperature of the molten pool in case (b) is relatively low, and voids appear. Since evaporation in the model occurs only at the computational grid located at the free surface. The non-surface high temperature (over boiling point) melt also evaporate after the surface melt evaporates. Therefore, the non-surface high temperature melt can persist for a period of time. As a result, it is reasonable to have the instantaneous temperature of the melt above the boiling point in the simulation. In addition, the electron beam has high energy efficiency and a preheating process that allows the EBSM molten pool to rise quickly to remarkably high temperatures. Thus, temperatures much higher than the boiling point are obtained in the simulations.

Increasing the preheating temperature can improve the thermal conductivity and thus the heat transfer efficiency of the electron beam-material interaction (Zhao et al., 2020). Therefore, increasing the preheating temperature facilitates the reduction of defects. Figure 10C shows the molten pool at standard atmospheric pressure (101,325 Pa) with preheating. According to Equation (13), vapor recoil pressure is highly dependent on atmospheric pressure. Low chamber pressure produces a feeble metal vapor recoil, and the evaporation has a weak counter-impact on the liquid surface.

The high ambient pressure in case (c) significantly exacerbated the effect of the recoil pressure on the molten pool surface. Under standard atmospheric pressure, a depression appeared on the surface of the molten pool and deepened continuously. During the scanning process, spatter was generated, and the liquid metal fell onto the surrounding powder, leading to internal mass loss and surface irregularities in the molten pool. Due to the instability of the molten pool, the accumulated heat is effectively dissipated, and the instantaneous maximum temperature of the molten pool is much lower than that under vacuum conditions. The distribution of pressure on the molten pool during melting and solidification under the three environmental conditions is shown in Figure 10D. Under vacuum conditions, the pressure was kept below 10^7 Pa and was even lower without preheating. From Equation (13), the recoil pressure is also a function of temperature; therefore, a higher preheating temperature resulted in a higher recoil pressure. Under standard atmospheric pressure, the pressure was significantly higher, at least one order of magnitude greater than the pressure in vacuum. Because the ambient pressure is a critical factor in determining the vapor recoil pressure, the vacuum environment in EBSM not only enables the electron beam to avoid interference from impurities in the gas but also effectively suppresses defects.

4.3 Effect of process parameters

In addition to environmental conditions, the influence of process parameters on the morphology and quality of the molten pool during formation cannot be overlooked. For a single track, the line energy density ($E_L = P/V$) is commonly used to determine the energy input. Figure 11 illustrates the cross section and dimensions of the molten pool at the end of the scan for different E_L values. It is worth noting that the simulated beam spot diameter is 250 μm , which corresponds to the minimum diameter of the Arcam A2X machine. However, in the actual experiment, the beam spot diameter is primarily controlled by the “focus offset” ranging from -60 mA to 60 mA. The precise relationship between the beam spot diameter and the focus offset current used in processing has not been provided by Arcam; however, they are consistent, meaning that higher current values result in larger beam spot diameters. In this experiment, the current for the focus offset was set at 30 mA.

Figures 11A–D, as well as E, C, represent cases where either the scanning speed or power is kept constant while E_L is increased. Figures 11B, E, F represent cases where E_L is kept constant while power and scanning speed are increased. With an increase in E_L , the width and depth of the molten region processed by EBSM increase. Moreover, when E_L remains unchanged, the width of the molten pool becomes wider and the depth becomes smaller as power and scanning speed increase. Because EBSM tends to operate in conduction mode, the molten pool exhibits a large width-to-depth ratio, with the width expanding faster than the depth, displaying a wide and shallow characteristic. This is one of the reasons why EBSM achieves high deposition rates. Furthermore, different E_L values also impact the surface quality of the molten pool, as depicted in Figure 12. At lower E_L values (Figure 12A), insufficient fusion of the powder and substrate occurs, resulting in

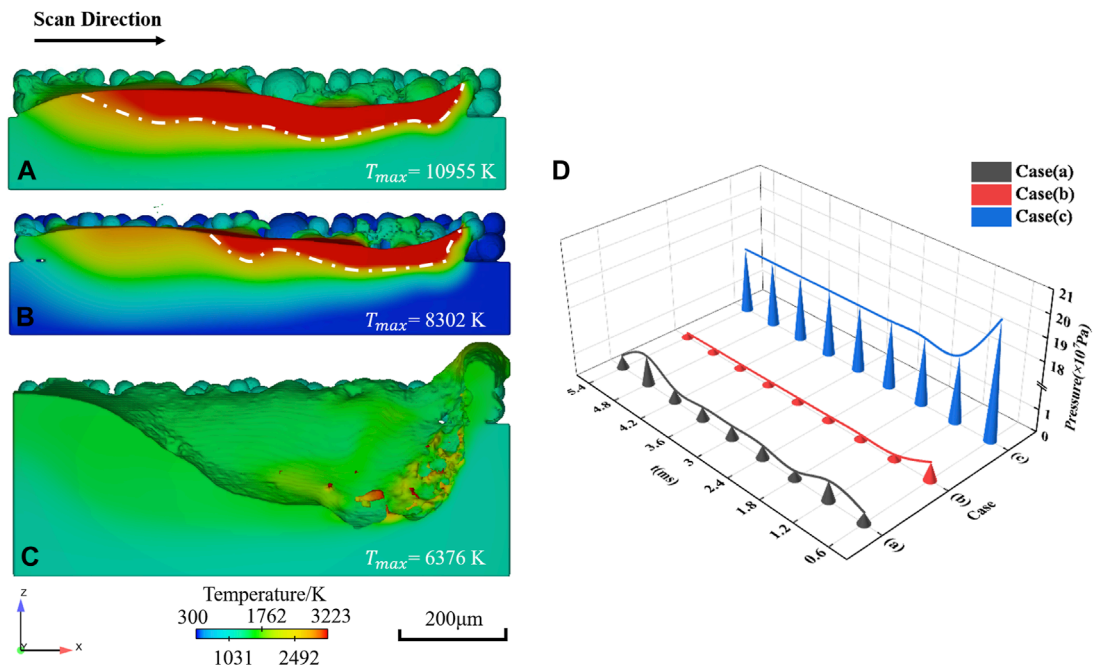


FIGURE 10 Effect of environmental conditions on molten pool morphology and temperature field. (A) Vacuum (0.1 Pa) with preheating (1273 K), (B) vacuum without preheating (300 K) and (C) standard atmospheric pressure (101,325 Pa) with preheating. (D) The pressure under different ambient conditions.

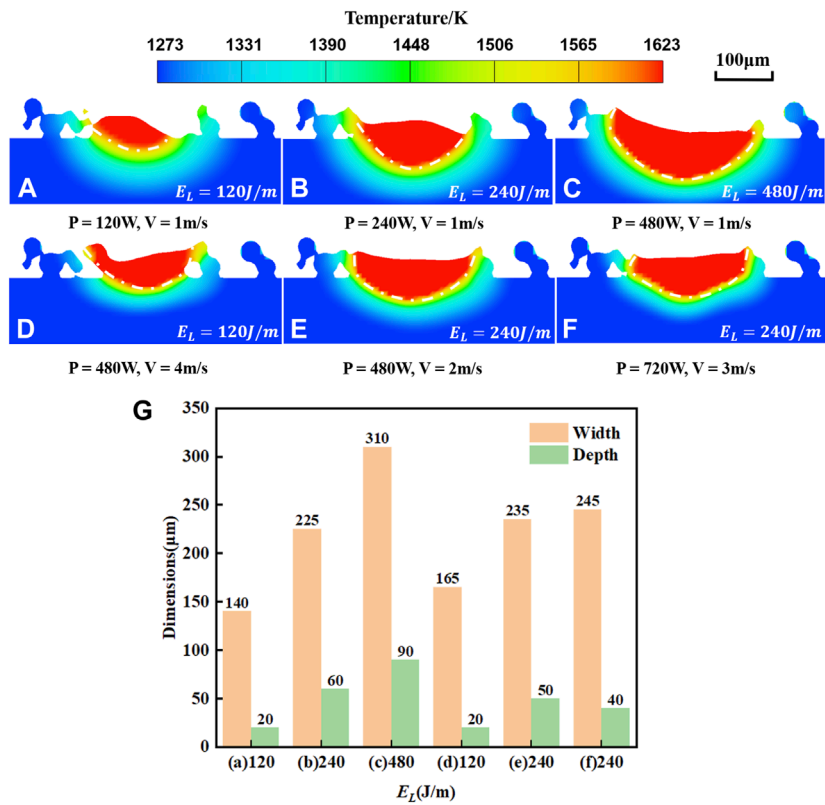


FIGURE 11 Cross-section view of the molten pool at different E_L . (A–F). (G) Molten pool dimensions in width and depth.

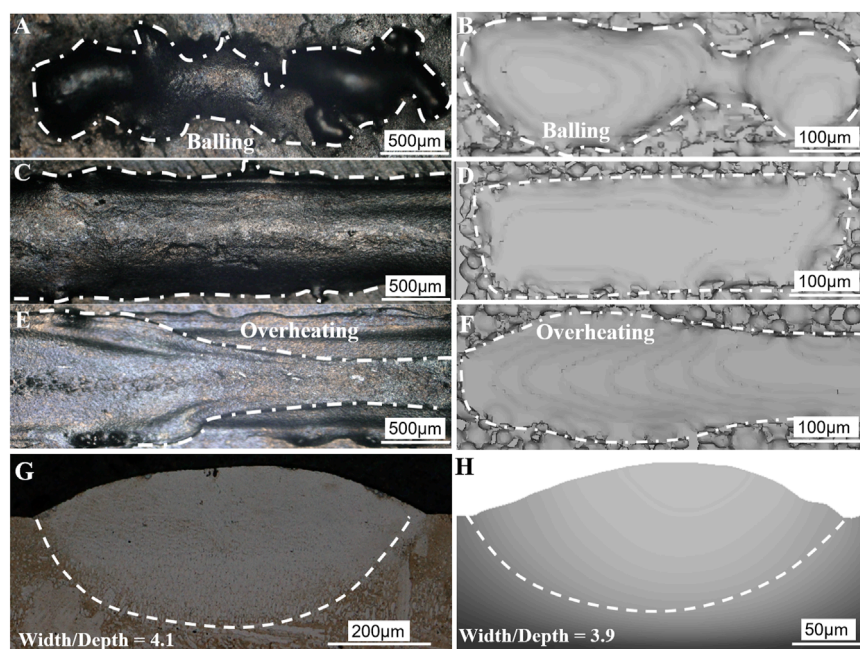


FIGURE 12

Surface morphologies of the melted tracks from experiments (left) and corresponding simulations (right) with different E_L : (A, B) 120 J/m, (C, D) 240 J/m and (E, F) 480 J/m. (G, H) The molten pool cross section for both simulation and experiment show a large width/depth ratio. The gray color indicates that the molten pool has solidified.

balling due to surface tension. At higher E_L values (Figure 12E), excessive heat leads to significant fluctuations and unevenness on the molten pool surface, with ablation occurring in the middle.

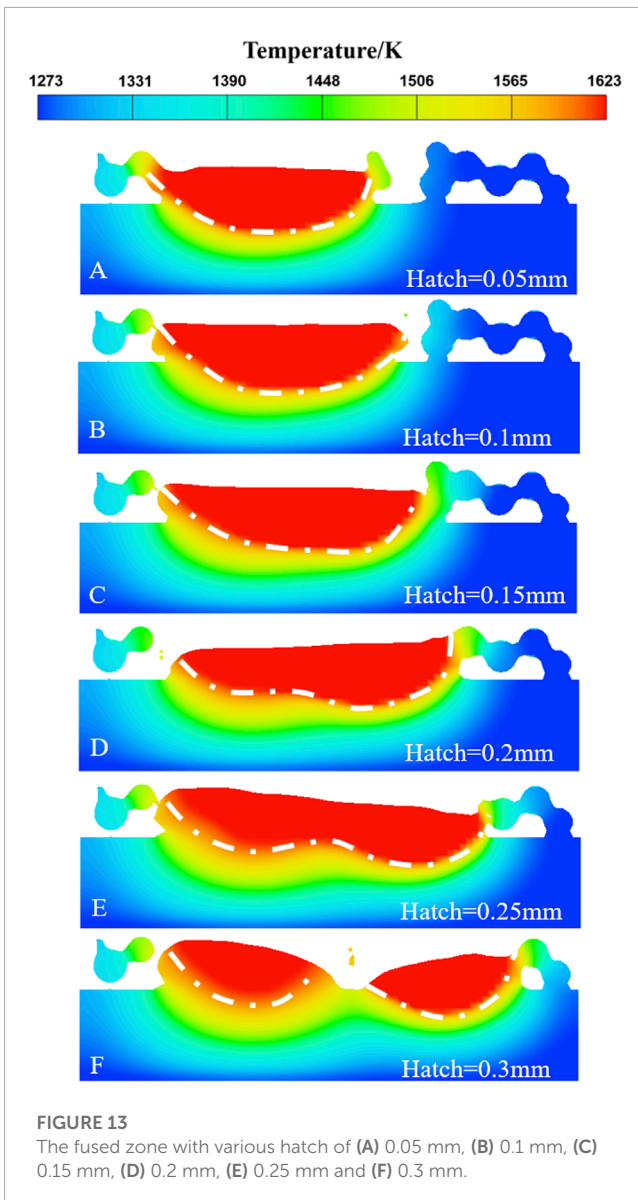
Once the spot diameter has been determined (250 μm in the simulation), our main concern is to identify the E_L value at which the size of the molten pool can reach or exceed the spot diameter. This ensures that the input energy is appropriately matched to the setup. Through a series of simulations, we found that a minimum E_L of 300 J/m is required to achieve a satisfactory melt pool width. However, as mentioned earlier, the beam spot diameter in the experimental setup is unknown. Although the experimental beam spot diameter is much larger than the simulated ones, all the cross-sections of the molten pool exhibit a significant width-to-depth ratio, as shown in Figure 12. This is in stark contrast to the narrow and deep cross-sections of the molten pool observed by Wang et al (Wang et al, 2022) in SLM.

In addition to power and scanning velocity, hatch is another crucial process parameter. The heat source exhibits a wide variation in the horizontal direction, resulting in a density distribution of heat flow that prompts the molten pool morphology to display a deep middle and shallow ends trend horizontally. If the molten pool does not overlap sufficiently, gaps may appear between the solidified tracks, negatively impacting the final quality of the printed part. Therefore, proper overlap is essential in EBSM to ensure track continuity, prevent defects during solidification, and reduce cracks. In actual production, the hatch is consistently smaller than the beam spot to achieve well-formed parts. To investigate the effect of hatch,

simulations were conducted with hatch sizes of 0.05 mm, 0.1 mm, 0.15 mm, 0.2 mm, 0.25 mm, and 0.3 mm, as shown in Figure 13. It was observed that when the hatch exceeded 0.15 mm, the melted region of the first track did not extend as much as the second track. The heat in the molten pool was insufficient to sustain its expansion, indicating the occurrence of solidification. As the hatch size continued to increase, a discontinuity appeared at the bottom of the molten pool until complete separation occurred at a hatch size of 0.3 mm. This significantly impacts the part's quality and can even result in unsuccessful printing. Therefore, when aiming to achieve better fusion of multiple tracks, the hatch size should not be too large, as it would not significantly increase the processing time.

To further understand the impact of hatch size on part quality, several cuboid samples were produced with hatch sizes of 0.05 mm, 0.1 mm, 0.15 mm, and 0.2 mm under the same energy density. Figure 14 illustrates three-dimensional surface topographical images of these samples. The samples exhibited an uneven surface due to excessive melting under a hatch size of 0.05 mm. Excessive melting caused by overheating or slow heat dissipation leads to an oversized molten pool that persists for a prolonged period (Wits et al, 2016).

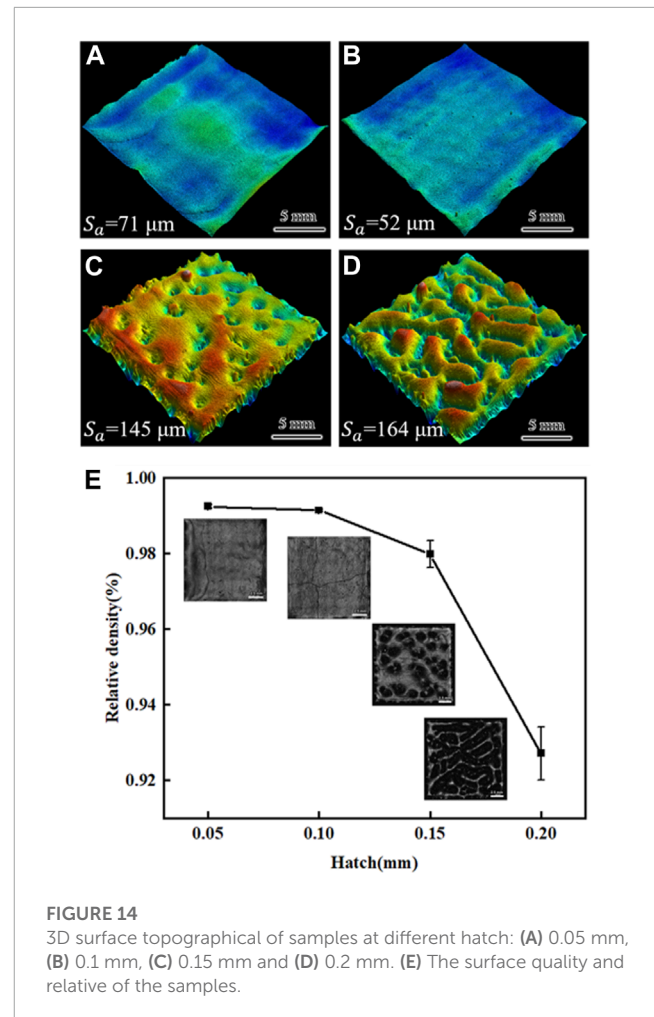
Protrusions and depressions appear on the solidified surface due to surface tension. In contrast, for the samples built with a hatch of 0.1 mm, the surface was relatively flat; however, noticeable cracks were present. These cracks are caused by the high Ti and Al content of the superalloy, which is beyond the scope of this paper. Relevant studies on this topic can be found in the



literature, such as (Chen et al, 2018) (Xu et al, 2018) (Grange et al, 2020) (Taheri, 2021). However, when the hatch was increased to 0.15 mm and 0.2 mm, the surface of the samples exhibited unfused porous morphological features with large voids. Insufficient penetration of the molten pool, which is directly related to the hatch distance and inadequate energy input, results in a lack of fusion.

The relative densities of the as-built samples were evaluated using the Archimedes method, as shown in Figure 14E. The density of the samples decreased as the hatch distance increased. When the line energy density is the same, a smaller hatch distance corresponds to a larger volume energy density. Therefore, as the volume energy continued to increase, the density reached a stable value.

The present study focused on the dynamics of single/double tracks molten pools and the factors influencing them in EBSM. Thus, this study is limited as the simulations were performed in a



single layer. In future studies, we plan to investigate the influence of multi-layer printing on the molten pool.

5 Conclusion

In this study, the flow behavior of the molten pool and influencing factors of EBSM of IN738 alloy were investigated through DEM and CFD simulations and experimental analysis. The main conclusions are: Gusarov et al, 2003.

- (1) The EBSM molten pool tends to maintain the conduction mode of the melting process. Due to the high energy absorption rate, preheating temperature, and vacuum environment, the molten pool continues to expand even after the end of the scan, exhibiting a “fast heating, slow cooling” trend throughout the printing process.
- (2) Driven by Marangoni force, the molten pool rapidly flows backward from the high-temperature region to the low-temperature region after the beam spot, returns and collides in the central region, producing vortices that converge and flow upward. Throughout the flow process, the flow velocity at the irregular solid-liquid interface is much higher than inside the molten pool.

- (3) The simulated temperature field shows that the instantaneous maximum temperature of the molten pool during melting is much higher than the material's boiling point. The recoil pressure mainly contributes to the molten pool shape. However, under vacuum, the recoil pressure is considerably lower than that at standard atmospheric pressure, and increasing the preheating temperature increases the recoil pressure.
- (4) The width and depth of the molten pool expand as the E_L increases, and higher power and scanning velocity make the width/depth ratio larger. The hatch mainly affects the relative density and surface quality of the sample. A large hatch distance tends to result in inadequate fusion and a porous morphological feature.

Data availability statement

The original contributions presented in the study are included in the article/[Supplementary Material](#), further inquiries can be directed to the corresponding authors.

Author contributions

YZ: methodology, investigation, writing. XF: investigation, supervision. WZ: investigation, review and editing. WG: conceptualization, resources. ZW: supervision, review and editing. JZ: project administration, supervision. All authors contributed to the article and approved the submitted version.

References

- Al-Bermani, S. S., Blackmore, M. L., Zhang, W., and Todd, I. (2010). The origin of microstructural diversity, texture, and mechanical properties in electron beam melted Ti-6Al-4V. *Metallurgical Mater. Trans. a* 41 (13), 3422–3434. doi:10.1007/s11661-010-0397-x
- Allmen, M. V., and Blatter, A. (2013). *Laser-beam interactions with materials: Physical principles and applications*. 2. Berlin: Springer Science & Business Media.
- Aune, R. E., Battezzati, L., Brooks, R., Egry, I., and Queded, P. N. (2005). "Thermophysical properties of IN738LC, MM247LC and CMSX-4 in the liquid and high temperature solid phase[J]," in International Symposium on Superalloys & Derivatives Location, Pittsburgh Pa, October 2005.
- Boley, C. D., Khairallah, S. A., and Rubenchik, A. M. (2015). Calculation of laser absorption by metal powders in additive manufacturing. *Appl. Opt.* 54 (9), 2477–2482. doi:10.1364/ao.54.002477
- Chapman, L., Morrell, R., Queded, P. N., Brooks, R. F., Brown, P., Chen, L. H., et al. (2008). Properties of alloys and moulds relevant to investment casting. *NPL Rep. MATC*. 141.
- Chen, K. C., Chen, T. C., Shiue, R. K., and Tsay, L. W. (2018). Liquation cracking in the heat-affected zone of IN738 superalloy weld. *Metals* 8 (6), 387. doi:10.3390/met8060387
- Cheng, Bo, and Chou, Kevin (2013). "Melt pool geometry simulations for powder-based electron beam additive manufacturing," in 2013 International Solid Freeform Fabrication Symposium, Austin, August 12–14, 2013 (University of Texas at Austin).
- Cheng, B., Loeber, L., Willeck, H., Hartel, U., and Tuffile, C. (2019). Computational investigation of melt pool process dynamics and pore formation in laser powder bed fusion. *J. Mater. Eng. Perform.* 28 (11), 6565–6578. doi:10.1007/s11665-019-04435-y
- Cho, Jung-Ho, Farson, D. F., Milewski, J. O., and Hollis, K. J. (2009). Weld pool flows during initial stages of keyhole formation in laser welding. *J. Phys. D Appl. Phys.* 42 (17), 175502. doi:10.1088/0022-3727/42/17/175502
- Chun, Yu Li (2019). Simulation and analysis on utilization ratio of laser cladding powder based on EDEM [J]. *J. Fujian Univ. Technol.* 17 (6), 6.
- Grange, D., Bartout, J. D., Macquaire, B., and Colin, C. (2020). Processing a non-weldable nickel-base superalloy by selective laser melting: Role of the shape and size of the melt pools on solidification cracking. *Materialia* 12, 100686. doi:10.1016/j.mta.2020.100686
- Gusarov, A. V., Laoui, T., Froyen, L., and Titov, V. (2003). Contact thermal conductivity of a powder bed in selective laser sintering. *Int. J. Heat Mass Transf.* 46 (6), 1103–1109. doi:10.1016/s0017-9310(02)00370-8
- Hirt, C. W., and Nichols, B. D. (1981). Volume of fluid (VOF) method for the dynamics of free boundaries. *J. Comput. Phys.* 39 (1), 201–225. doi:10.1016/0021-9991(81)90145-5
- Kerrouault, N. (2000). *Fissuration a chaud en soudage d'un acier inoxydable austénitique*. Paris: Châtenay-Malabry, Ecole centrale de Paris.
- Khairallah, Saad A., Anderson, A. T., Rubenchik, A., and King, W. E. (2016). Laser powder-bed fusion additive manufacturing: Physics of complex melt flow and formation mechanisms of pores, spatter, and denudation zones. *Acta Mater.* 108, 36–45. doi:10.1016/j.actamat.2016.02.014
- Khairallah, S. A., and Anderson, A. (2014). Mesoscopic simulation model of selective laser melting of stainless steel powder. *J. Mater. Process. Technol.* 214 (11), 2627–2636. doi:10.1016/j.jmatprotec.2014.06.001
- Körner, Carolin, Attar, Elham, and Peter, Heil (2011). Mesoscopic simulation of selective beam melting processes. *J. Mater. Process. Technol.* 211 (6), 978–987. doi:10.1016/j.jmatprotec.2010.12.016
- Leung, C. L. A., Tosi, R., Muzangaza, E., Nonni, S., Withers, P. J., and Lee, P. D. (2019). Effect of preheating on the thermal, microstructural and mechanical properties of selective electron beam melted Ti-6Al-4V components. *Mater. Des.* 174, 107792. doi:10.1016/j.matdes.2019.107792
- Lee, Y. S., and Zhang, W. (2016). Modeling of heat transfer, fluid flow and solidification microstructure of nickel-base superalloy fabricated by laser powder bed fusion. *Addit. Manuf.* 12, 178–188. doi:10.1016/j.addma.2016.05.003

Funding

This work was supported by the Young Elite Scientists Sponsorship Program by CAST (2021QNRC001) and the State Key Laboratory of Long-life High Temperature Materials (DECSKL202104).

Conflict of interest

The authors declare that the research was conducted in the absence of any commercial or financial relationships that could be construed as a potential conflict of interest.

Publisher's note

All claims expressed in this article are solely those of the authors and do not necessarily represent those of their affiliated organizations, or those of the publisher, the editors and the reviewers. Any product that may be evaluated in this article, or claim that may be made by its manufacturer, is not guaranteed or endorsed by the publisher.

Supplementary material

The Supplementary Material for this article can be found online at: <https://www.frontiersin.org/articles/10.3389/fmats.2023.1211648/full#supplementary-material>

- Li, E., Zhou, Z., Wang, L., Zou, R., and Yu, A. (2022). Numerical studies of melt pool and gas bubble dynamics in laser powder bed fusion process. *Addit. Manuf.* 56, 102913. doi:10.1016/j.addma.2022.102913
- Murr, L. E., Gaytan, S. M., Ceylan, A., Martinez, E., Martinez, J., Hernandez, D., et al. (2010). Characterization of titanium aluminide alloy components fabricated by additive manufacturing using electron beam melting. *Acta mater.* 58 (5), 1887–1894. doi:10.1016/j.actamat.2009.11.032
- Parteli, E. J., and Pöschel, T. (2016). Particle-based simulation of powder application in additive manufacturing. *Powder Technol.* 288, 96–102. doi:10.1016/j.powtec.2015.10.035
- Qi, H. B., Yan, Y. N., and Zhang, R. J. (2007). Scanning method of filling lines in electron beam selective melting. *Proc. Institution Mech. Eng. Part B J. Eng. Manuf.* 221 (12), 1685–1694. doi:10.1243/09544054jem913
- Riedlbauer, D., Scharowsky, T., Singer, R. F., Steinmann, P., Körner, C., and Mergheim, J. (2017). Macroscopic simulation and experimental measurement of melt pool characteristics in selective electron beam melting of Ti-6Al-4V. *Int. J. Adv. Manuf. Technol.* 88 (5), 1309–1317. doi:10.1007/s00170-016-8819-6
- Risse, J., and Broeckmann, C. (2019). *Additive manufacturing of nickel-base superalloy IN738lc by laser powder bed fusion[R]*. Aachen, Germany: Lehrstuhl für Lasertechnik.
- Shen, N., and Chou, K. (2012). “Numerical thermal analysis in electron beam additive manufacturing with preheating effects,” in 2012 International Solid Freeform Fabrication Symposium, Hilton, August 14–16, 2012 (University of Texas at Austin).
- Taheri, M. (2021). Analysis of solidification and liquation cracks in the electron beam welding of IN738 superalloy. *Metallogr. Microstruct. Analysis* 10 (6), 815–822. doi:10.1007/s13632-021-00793-z
- Tan, X., Kok, Y., Tan, Y. J., Descoins, M., Mangelinck, D., Tor, S. B., et al. (2015). Graded microstructure and mechanical properties of additive manufactured Ti-6Al-4V via electron beam melting. *Acta Mater.* 97, 1–16. doi:10.1016/j.actamat.2015.06.036
- Tumbleston, J. R., Shirvanyants, D., Ermoshkin, N., Januszewicz, R., Johnson, A. R., Kelly, D., et al. (2015). Continuous liquid interface production of 3D objects. *Science* 347 (6228), 1349–1352. doi:10.1126/science.aaa2397
- Wang, W., Lin, W., Yang, R., Wu, Y., Li, J., Zhang, Z., et al. (2022). Mesoscopic evolution of molten pool during selective laser melting of superalloy Inconel 738 at elevating preheating temperature. *Mater. Des.* 213, 110355. doi:10.1016/j.matdes.2021.110355
- Wang, Xiaoqing, Gong, Xibing, and Chou, Kevin (2015). Scanning speed effect on mechanical properties of Ti-6Al-4V alloy processed by electron beam additive manufacturing. *Procedia Manuf.* 1, 287–295. doi:10.1016/j.promfg.2015.09.026
- Wits, W. W., Bruins, R., Terpstra, L., Huls, R. A., and Geijselaers, H. (2016). Single scan vector prediction in selective laser melting. *Addit. Manuf.* 9, 1–6. doi:10.1016/j.addma.2015.12.001
- Xiang, Z., Yin, M., Deng, Z., Mei, X., and Yin, G. (2016). Simulation of forming process of powder bed for additive manufacturing. *J. Manuf. Sci. Eng.* 138 (8), 081002. doi:10.1115/1.4032970
- Xu, J., Lin, X., Zhao, Y., Guo, P., Wen, X., Li, Q., et al. (2018). HAZ liquation cracking mechanism of IN-738lc superalloy prepared by laser solid forming. *Metallurgical Mater. Trans. A* 49 (10), 5118–5136. doi:10.1007/s11661-018-4826-6
- Yan, W., Qian, Y., Ge, W., Lin, S., Liu, W. K., Lin, F., et al. (2018). Mesoscale modeling of multiple-layer fabrication process in Selective Electron Beam Melting: Inter-layer/track voids formation. *Mater. Des.* 141, 210–219. doi:10.1016/j.matdes.2017.12.031
- Yann, D., Lacoste, E., and Arvieu, C. (2010). Numerical modeling of inconel 738LC deposition welding: Prediction of residual stress induced cracking. *J. Mater. Process. Technol.* 210 (14), 2053–2061. doi:10.1016/j.jmatprotec.2010.07.027
- Zäh, M. F., and Lutzmann, S. (2010). Modelling and simulation of electron beam melting. *Prod. Eng.* 4 (1), 15–23. doi:10.1007/s11740-009-0197-6
- Zhao, Y., Koizumi, Y., Aoyagi, K., Wei, D., Yamanaka, K., and Chiba, A. (2019). Molten pool behavior and effect of fluid flow on solidification conditions in selective electron beam melting (SEBM) of a biomedical Co-Cr-Mo alloy. *Addit. Manuf.* 26, 202–214. doi:10.1016/j.addma.2018.12.002
- Zhao, Y., Aoyagi, K., Yamanaka, K., and Chiba, A. (2020). Role of operating and environmental conditions in determining molten pool dynamics during electron beam melting and selective laser melting. *Addit. Manuf.* 36, 101559. doi:10.1016/j.addma.2020.101559